International Journal of Pressure Vessels and Piping 206 (2023) 105078

Contents lists available at ScienceDirect

International Journal of Pressure Vessels and Piping

journal homepage: www.elsevier.com/locate/ijpvp

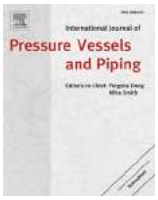

Comprehensive microstructural and mechanical characterization of transient liquid phase bonded austenitic stainless steel by Ni–Cr–Si–B amorphous interlayer

M. Naalchian, M. Kasiri-Asgarani **, H.R. Bakhsheshi-Rad *, J. Manshaee

Advanced Materials Research Center, Department of Materials Engineering, Najafabad Branch, Islamic Azad University, Najafabad, Iran

ARTICLE INFO

Keywords:
Transient liquid phase bonded austenitic stainless steel
Amorphous interlayer
Microstructural
Mechanical property

ABSTRACT

In this research, along with the joining of the gas turbine fuel nozzle part from austenitic stainless steel 316L alloy with BNi-2 interlayer by the transient liquid phase bonding process, microstructure test, shear strength and tensile strength tests have been placed. Bonding at a temperature of 1080 °C and a holding time of 45 min has led to the completion of isothermal solidification in the bonding zone. Microstructural and phase investigations showed that austenitic stainless steel 316L undergoes phase transformation after exposure to temperature conditions and the δ ferrite phase is formed as separate areas due to the diffusion of the solid state of ferrite-forming elements, and the grains of the base metal are 32 μm have reached 43 μm, which has caused a decrease in the shear strength of the base metal from 362 MPa to 347 MPa. Despite the completion of isothermal solidification in the joint centerline due to the boron diffusion of the solid state into the base metal and achieving the maximum shear strength of the joint (402 MPa), two generations of boride deposits have been formed. The first-generation borides based on nickel-iron-chromium-molybdenum are formed during heating up to the bonding temperature, and the second-generation boride deposits are based on iron-chromium-molybdenum, which were deposited in situ during the isothermal solidification stage. The microhardness test confirms the uniform distribution of hardness in each of the bonding zones, which feedback was determined in the tensile strength test. The tensile strength of the bonded sample was 485 MPa, which is approximately 82 % of stainless steel 316L. In both shear and tensile tests, the presence of small dimples indicates the ductile failure of the joint samples in base metal.

1. Introduction

Among the large family of steels, stainless steels are widely used because of their variety of structural properties [1]. Corrosion resistance, high tensile strength, high durability, temperature resistance, ease of deformation, and mass manufacturing capabilities are some of the most crucial characteristics of stainless steel [2]. Among the five well-known families of stainless steels (austenitic, ferritic, martensitic, precipitation-hardening, and duplex), the austenitic family of stainless steels (group 300) is designed for applications that require excellent corrosion resistance and good performance at high and low temperatures (and even below zero) [3]. Austenitic stainless steel 316L was created by adding molybdenum to austenitic stainless steel 304L/304, improving its corrosion resistance in medium corrosive environments. This alloy has high resistance to chloride pitting corrosion [4]. Due to its good structural stability, 316L austenitic stainless steel is used in heat exchangers, pumps, pressure vessels, chemical plants, power generation, food storage tanks, medical implants, marine structures, food processing equipment and textiles [5].

This alloy is used either alone or in combination with other alloys to create a variety of industrial equipment, such as the structural components of land and air gas turbines, high-temperature engines, and exhaust parts [6,7]. Stage 1 shroud in 7B gas turbines was made by General Electric Corporation using 316 stainless steel with an oxidation-resistant coating [8]. Nuclear power facilities and aerospace sector equipment are both built using a mix of austenitic stainless steel 316L and Inconel 718 superalloy. For instance, Alstom Power Sweden has produced turbine engines using the 316L/718 dissimilar joint [9]. According to Sashank et al. [10] investigation of austenitic stainless steel to martensitic joints in atomic applications, dissimilar joints between

* Corresponding author. Advanced Materials Research Center, Department of Materials Engineering, Najafabad Branch, Islamic Azad University, Najafabad, Iran.
** Corresponding author.
E-mail addresses: m.kasiri@pmt.iaun.ac.ir (M. Kasiri-Asgarani), rezabakhsheshi@gmail.com, rezabakhsheshi@pmt.iaun.ac.ir (H.R. Bakhsheshi-Rad).

https://doi.org/10.1016/j.ijpvp.2023.105078
Received 4 September 2023; Received in revised form 10 October 2023; Accepted 16 October 2023
Available online 21 October 2023

austenitic and martensitic stainless steel are required in steam carrying pipes, headers, superheaters and reaction tubes in order to meet strength, cost, production, and service requirements. They claimed that in nuclear applications, nickel-based filler metals might be utilized to link P91ferritic/martensitic steel with 316 austenitic stainless steel. Dissimilar joints of Inconel 625 and stainless steel 316 are used in chemical processing equipment at high-temperature, especially in chromic acid calcining procedures [11].

One of the frequent issues during procedures when some heating occurs in various ways and for different causes is hot cracking in austenitic stainless steels. A form of cracking known as hot tearing happens during hot operations such as melting, casting or welding. In the welding of austenitic stainless steels, a variety of hot cracking may happen: A molten phase in the molten zone causes solidification cracking (Supersolidus cracking), liquation cracking in the heat-affected zone, which is accompanied by melting in the grain boundaries, and solidification cracking in the weld metal, which is more common and more destructive than the other two types of cracking [12]. Kujanpaa et al. [13] examined solidification cracking in austenitic stainless steels by using a spot-varestraint test with laboratory and industrial heating. They stated that the development of solidification grain boundaries, interfacial phase energy and phase transformation that take place during solidification govern the nucleation and propagation of solidification cracks. They claimed that crack nucleation is brought on by certain austenitic alloys' early solidification austenitic condition. Sulfur as an impurity might exacerbate the solidification cracking condition. Ferrite-austenite solidification (FA) mode inhibits the nucleation and propagation of cracks during solidification. Cracks that are formed during solidification may readily be filled with melts of filler metal.

Although the brazing process does not have the problems mentioned above that are present in fusion welding processes, the strength of the joint can still be as strong as the base metal because intermetallic compounds present in the brazing process are susceptible to crack initiation and propagation has no existence. Kemmenoe et al. [14] are investigated the strength of joints by lap configuration design of stainless steel 316 that brazed by nickel-based amorphous foils (MBF-20, MBF-51, and MBF-67) containing elements that lower the melting points of boron, silicon, and phosphorus at 1090 $^{\circ}C$/15 min condition. The results of the mechanical and microstructural examinations of the joints revealed that the hard microconstituent particles in the joints were to blame for the joint fracture. These particles lessen the flexibility as well as the strength of the brazed specimen. Additionally, by producing high residual stresses (through differential thermal contraction), these pseudo-eutectic hard particles that compounds rich in nickel-boron, chromium-boron, and nickel-chromium-phosphorus cause stress concentration in the elastic and plastic discontinuity and reduce the Adhesion and cohesion the joint and finally failure happens along these hard particles. In a different study, Zhang et al. [15] brazed the high Nitrogen austenitic stainless steel by Ni–Cr–P based filler metal at 950, 1000, and 1050 °C for a holding time of 20 min. The microstructural analysis revealed that at the aforementioned joining temperatures, $(Ni, Cr)_3P$ compounds are continuously formed in the centerline of the bond, and Cr_2N compounds are composed at the bonding zone/stainless steel interface. As the temperature rises, their volume decreases and the shear strength of the joint increases. Due to the lack of Cr_2N formation in the joint and the reduction of $(Ni, Cr)_3P$, the sample at 1050 °C/20 min has the best shear strength (163 MPa).

If the holding time at the joining temperature is prolonged enough, elements that reduce the melting point of the filler metal (such as boron, silicon, phosphorus, and carbon) can diffuse to the base metals in the molten state and their amount in the joint is reduced to such an extent that it becomes less than the amount required for the formation of destructive and brittle intermetallic compounds. Thus, it is possible to achieve a single-phase solid solution joint. This step, which is known as isothermal solidification, is the basis of the transient liquid phase bonding process or diffusion brazing [16]. Emami et al. [17] investigated the microstructure formation mechanism and solidification sequence in the joint by transient liquid phase bonding Inconel 718 superalloy to stainless steel 316L with a 2-BNi interlayer at temperatures between 1030 °C and 1110 °C and holding times between 1 and 30 min. They claimed that limited storage durations result in the formation of hard borides rich in nickel and chromium, such as Ni_3B/Ni_2B and CrB/Cr_2B_3, which would have a negative impact on corrosion and mechanical qualities at high-temperatures. The single-phase area rich in nickel (γ - Ni) will, however, continue to develop in the joint when holding time is increased, which improves the mechanical characteristics (especially shear strength). Besides increasing the holding time, another important variable is the bonding temperature. Increasing the bonding temperature before the critical temperature (the maximum temperature above which increasing the holding time cannot decrease the isothermal solidification time [18]) can be effective in reaching a reasonable holding time in the isothermal solidification stage. Tazkieh et al. [19] stated that in the transient liquid phase bonding of Inconel 939 superalloy with BNi-2 interlayer, they found that increasing the bonding temperature (1060, 1120 and 1180 °C) at a constant holding time (45 min) can make athermal solidification zone (ASZ) as completely removed and created a complete isothermal solidification zone free of continuous eutectic compounds. This issue has caused a uniform distribution of elements along the joint seam, which has resulted in an increase in joint efficiency and shear strength in the jointed sample at 1180 °C/45 min condition.

Many fuel nozzles are often employed in gas turbines to inject fuel into the combustion chamber. These fuel nozzles are constructed from a number of components that are joined together using a brazing or welding procedure. The inability to master the inner components, residual stress and intrinsic welding issues in the fusion welding process, as well as the presence of several non-metallic compounds in the brazing process, make it challenging for the part to operate at high-temperatures.

To the best of the authors' knowledge, there is no published report regarding joining a multi-component fuel nozzle composed of austenitic stainless steel 316L together via a procedure known as transient liquid phase bonding (TLP). Thus, in this study, a multi-component fuel nozzle composed of austenitic stainless steel 316L is joined together via the TLP method (Fig. 1). Next to the nozzle, laboratory samples with standard dimensions are placed to check the microstructure, shear strength and tensile strength. Eventually, the details of TLP bonding joints are provided in the present study.

2. Materials and methods

2.1. Materials

The substrate for this study was a plate of austenitic stainless steel 316L. The chemical composition of the substrate was determined by the FOUNDRY-MASTER Pro2 model optical emission spectrometric analysis method that particularly calibrated stainless steels (Table 1). Amorphous filler metal BNi-2 is used as the bonding agent, whose chemical composition is listed in Table 2, along with its general characteristics.

2.2. Preparation and diffusion brazing

Austenitic stainless steel sheet 316L has been cut using a wire electric discharge machine to create samples that are 40 × 10 × 5 mm^3 in size. All of the sample surfaces were smoothed with sandpaper ranging from 60 to 1200, and the bonding surfaces were polished with water before being cleaned with distilled water and preserved in alcohol until the bonding. The samples with foil were cleaned ultrasonically for 1 h. A pressure of 0.3 MPa was then applied to the joint by screws after the samples were set in a heat-resistant austenitic stainless steel 310 holder with a full overlapping joint design, which is the interlayer between the adjacent surfaces of the joint (Fig. 2a). The joining process was carried

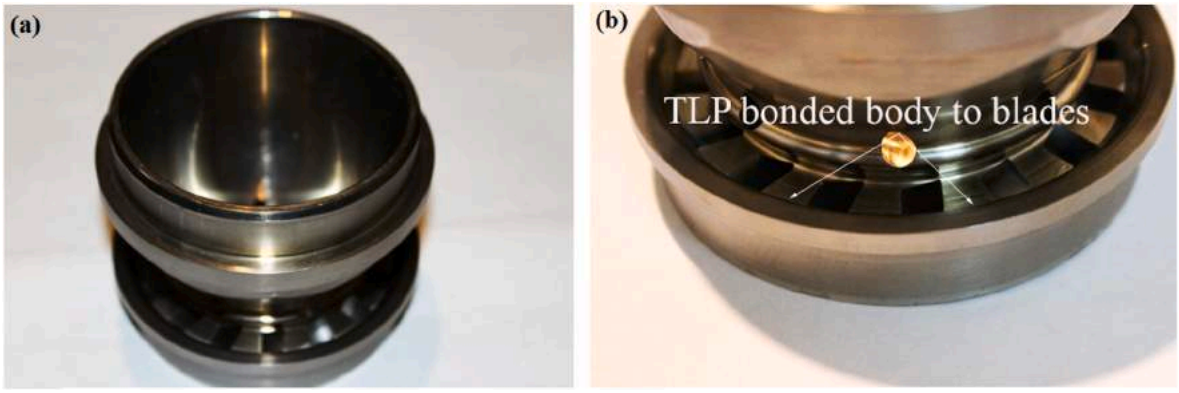

Fig. 1. a) Gas turbine fuel nozzle and b) Transient liquid phase (TLP) bonding of blade to body.

Table 1
Chemical composition of stainless steel 316L as base metal (wt.%).

Element	Fe	C	Cr	Ni	Mo	10
Content	Bal.	0.03	17	10.5	2.1	1.3

Table 2
Chemical composition (wt.%), solidus and liquidous temperature (°C) of nickel-based BNi-2 amorphous foil.

Element	Ni	Cr	Si	B	C	Fe	Solidus	Liquidous
Content	Bal.	7	4.5	3.2	0.06	1.5	959.2	1012.3

out in a vacuum furnace with a 10^{-6} torr vacuum. For diffusion brazing, a bonding temperature of 1080 °C and a holding time of 45 min have been used. The heating rate of the assembly was 10 °C/min, and it cools at a rate of 8 °C per minute. The transient liquid phase bonded sample has the 40 × 10 × 10 mm^3 size (Fig. 2b). It is cut according to Fig. 2c, subsequently, one sample for optical and electron metallography, one sample for hardness test and three samples for shear strength test were obtained.

The tensile test samples were made from round pieces of stainless steel 316 L that had a diameter of 10 mm and a length of 8 mm. A lathe was used to prepare the surfaces adjacent to the bond. To complete the bonding operation, a special holder is used, the design of which is shown in Fig. 3a. After degreasing, washing with alcohol and acetone, and placing the interlayer between the surfaces adjacent to the joint, three tensile test samples were tested under the same conditions as above (bonding temperature 1080 °C and holding time 45 min). The image of the tensile test samples after the bonding operation is shown in Fig. 3b.

2.3. Characterization

2.3.1. Microstructural and phase characterization

The cut samples were mounted with cold epoxy adhesive to retain their qualities and avoid abrupt changes brought on by heat, allowing for the best possible handling of their preparatory tasks. They were cleaned with distilled water and alcohol after being sanded using SiC sandpaper with numbers 60 to 3000. The samples were polished using a Struers polishing pad and 0.05 μm alumina after being polished with 1 μm alumina initially. With the use of 10 ml H_2O+10 ml HCl+10 ml HNO_3 and Murakami 100 ml H_2O+10gKOH+ 10g$K_3Fe(CN)_6$ solutions, the polished base and bonded metal samples were etched, respectively. The AxiotechZIESS optical microscope equipped with Clemex image analysis software was used for imaging, determining the size of the base metal grains and examining the extent of different zones of the bonded area. FEIAccura TM 850 field emission scanning electron microscope equipped with X-ray spectroscopy based on energy distribution (EDS) Oxford-Instrument INCA 400 X-Max model was used to evaluate the chemical composition in point, line and area mode. X-ray diffraction (XRD) patterns of the as-received were prepared with a PHILIPS PW 3040 with CuKα X-ray wavelength.

2.3.2. Mechanical characterization

2.3.2.1. Macro and microhardness measurements. Based on the ASTM E384 standard, macro and microhardness tests have been carried out. The base metal's variations in hardness both before and after the bonding have been examined using the macrohardness test. The hardness was measured using a Rockwell hardness tester (C scale) at 5 places, and the findings were then presented as an average. The microhardness distribution, which depicts the distribution of phases and constituents along the joint, was assessed using a microhardness test. Under a 10 g load, a Vickers Letizmicrohardness tester was used. The findings of the linear microhardness assessment conducted in 3 regions are presented as an average.

2.3.2.2. Shear strength testing. To investigate the room temperature shear strength of base metal in as-received, in heat treatment (1080 °C/45 min) conditions, and also the bonded samples, the shear test was used. To perform the shear test, a clamp was used to apply shear stress directly to the bonding line [20]. The test was performed according to the ASTM D1002 standard at a speed of 1 mm/min with a Universal device.

2.3.2.3. Tensile strength testing. A tensile test based on the ASTM E8 standard was performed to examine the tensile characteristics of the base metal samples of austenitic stainless steel 316L and bonded and the final samples depicted in Fig. 3c. After the machining process, the gage section was longitudinally sanded with 800 grit sandpaper to entirely remove the machining markings. It was carried out at room temperature at a speed of 1 mm/min using a Universal machine. The fracture surface of the samples was studied using a field emission scanning electron microscope to ascertain the mode and mechanism of failure after the shear strength and tensile strength tests were completed.

3. Results and discussion

3.1. Microstructure of base metals before heat treatment

Fig. 4 shows the microstructure of austenitic stainless steel 316L in as-received condition (rolled and annealed) at two magnifications of 50× and 200X. As can be seen, the microstructure of austenitic stainless steel 316L is a single phase with fine equiaxed distributed in the matrix. Fig. 5 depicts the stainless steel 316L X-ray diffraction pattern before

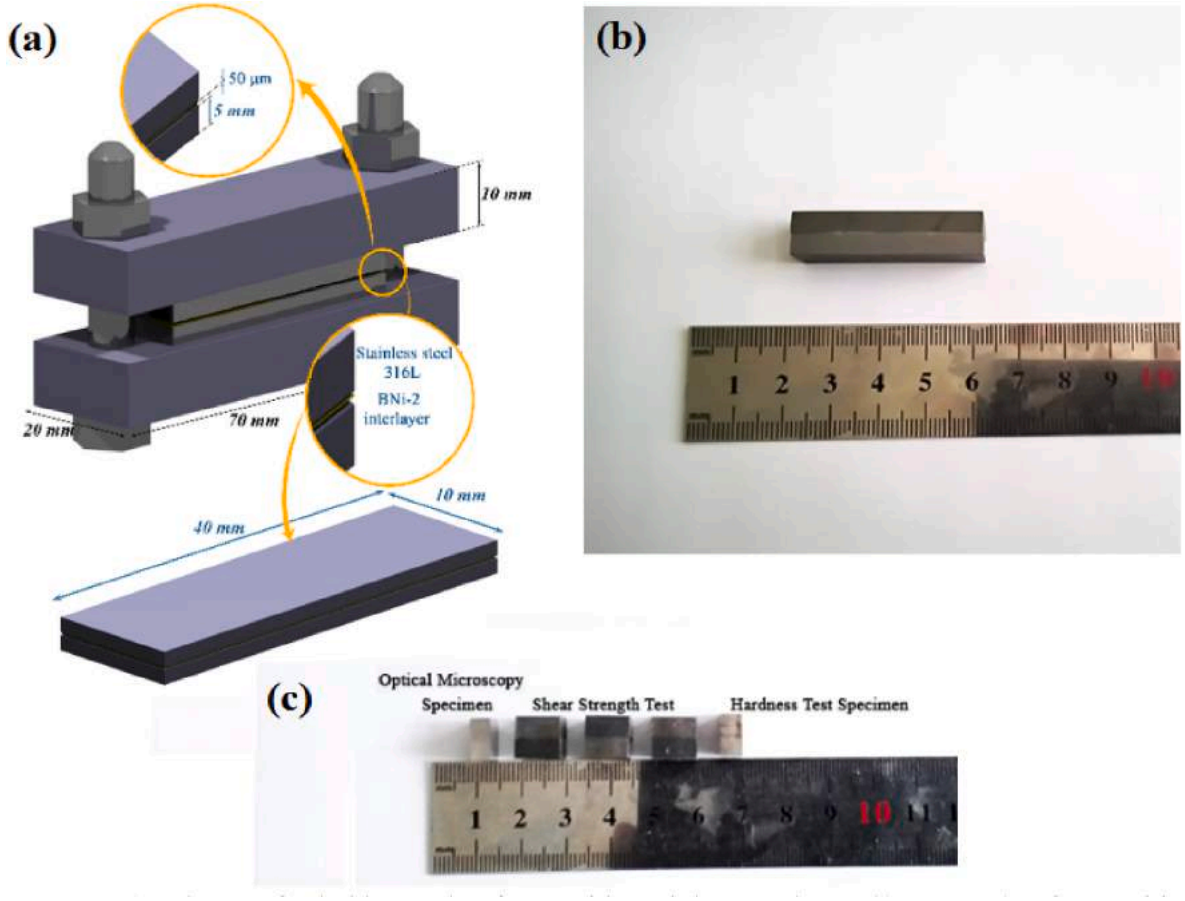

Fig. 2. a) Scheme of a holder made of austenitic stainless steel 310, b) A sample of austenitic stainless steel 316LTLP bonded under condition of 1080 °C for 45 min and c) A cut sample for optical and electronic metallographic tests, microhardness and shear strength testing.

heat treatment (joining). It is clear that the most diffraction from the plane (1 1 1), (0 0 2) and (0 2 2) is obtained from the Face Centered Cubic structure (FCC), which can be seen to be the dominant matrix of γ austenitic structure (solid solution). The quantity of ferrite in the microstructural measurements was so little that it could not be seen, but only one peak of the body-centered cubic structure from the (1 1 0) plane could be seen in the X-ray diffraction pattern. Based on the quasi-binary iron-nickel-chromium phase diagram, considering the position of austenitic stainless steel 316L on it and the ratio of equivalent chromium to equivalent nickel, it is possible to predict the phases formed during solidification of the alloy (or welding without filler metal). Austenitic stainless steel AISI316L, having a ratio of chromium equivalent to nickel equivalent to 1.71, has an Austenite-Ferrite (FA) solidification mode. That is, during cooling to room temperature, it passes through four phase regions, which from the highest to the lowest temperature are: L+δ+γ region, δ+γ region, pure austenite region and two-phase δ+γ region [21]. This means that δ+γ phases must be present at room temperature, but based on the X-ray diffraction pattern of the as-received sample (Fig. 5a), the amount of ferrite identified was very low; however, its presence cannot be denied. The average grain size is measured based on ASTM E12 standard, 32 μm. Some annealed twins are seen inside the grains, which are caused by rolling and annealing operations. The average value of microhardness of the background and the hardness of the mass in the base metal sample of 316L were measured around 176 HV_{10} and 31 HRC, respectively.

3.2. Microstructure evolution of base metal after heat treatment

Fig. 6 indicates the optical microscopy images of the microstructure of austenitic stainless steel 316L after exposure to 1080 °C for 45 min in two magnifications, 50× and 200X. It is completely clear that at this condition, the grain size of the base metal grew (43 μm), which is in terms of recrystallization during heat treatment [22], and the interesting thing is that the annealed twins are completely were omitted. Thus, the microstructure remains in the form of equiaxed grains. According to Fig. 6, it can be observed that the ferrite phase grew as dark areas in high magnification and can be determined. Fig. 5b indicates the X-ray diffraction pattern of the base metal sample heat-treated at 1080 °C for 45 min. In the X-ray diffraction pattern, the peak of the (1 1 0) plane, which is due to the δ ferrite phase, seems with higher intensity, and next to it, the peaks of the (2 0 0) and (2 1 1) planes are seen, which indicates the presence of the phase ferrite is δ. It seems that the presence of a very small amount of ferrite δ in the context of austenitic stainless steel 316L has acted as a nucleation site for the transformation of the austenite phase to ferrite. During heat treatment, the presence of molybdenum and chromium elements, which stabilize the ferrite phase, penetrated into the ferrite phase due to the solid state diffusion process and helped the growth of the ferrite phase. Therefore, it can be claimed that the presence of ferrite phase (even in very small amounts) acts as a well for the absorption of ferrite stabilizing elements [23]. Hardness in terms of grain growth and recrystallization is decreased to 26 HRC. It must be mentioned that the carbide peak ($M_{23}C_6$) was not identified in X-ray diffraction pattern. This part, which is formed through storage or slow cooling in the temperature range of 600–900 °C, has a destructive impact on the corrosion and mechanical properties of austenitic stainless steel 316L [24].

3.3. Microstructure of bonded zone

Fig. 7 shows the optical micrographs of the microstructure of TLP-

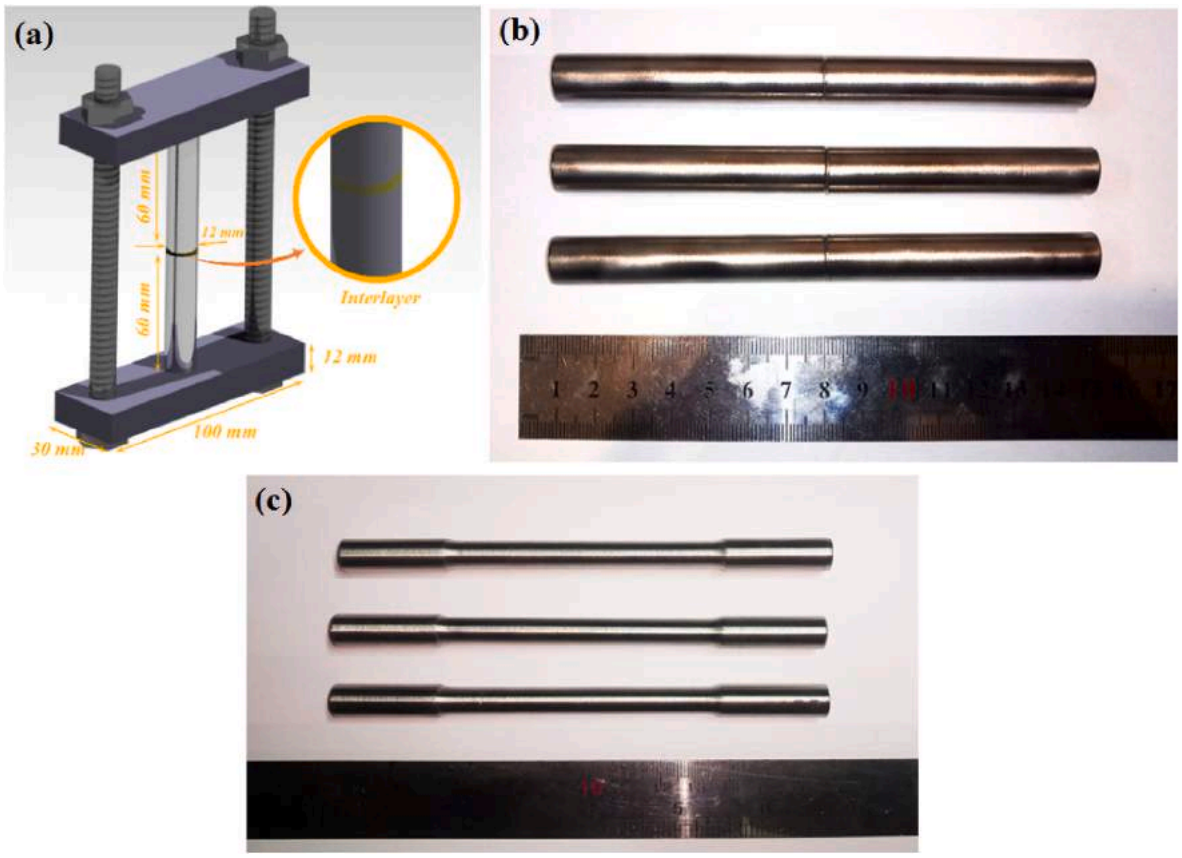

Fig. 3. a) The scheme of the holder for bonding the tensile strength test samples and b and c) The test samples bonded under the condition of 1080 °C for 45 min.

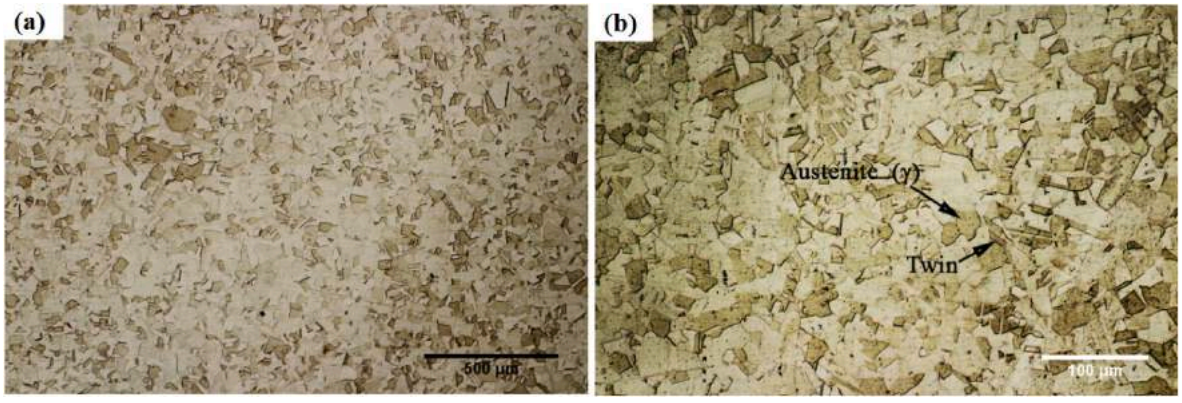

Fig. 4. Optical microscopy of austenitic stainless steel 316L at as-received condition at: a) 50X and b) 200× magnifications.

bonded austenitic stainless steel 316L by amorphous BNi-2 foil with a thickness of 50 μm with a holding time of 45 min at a bonding temperature of 1080 °C. This figure is prepared in two magnifications, ×50 and ×200, to show the microstructure of the base metal along with the microstructure of the joint. As can be seen in Fig. 7a, the bonding zone is clearly defined as a thin strip with a thickness of 52 μm in the centre, where stainless steel 316L is positioned at the top and bottom of the bonding zone. Fig. 7b demonstrates that the bonding zone is devoid of contaminants, holes, cracks, and harmful compounds, such as those with a low melting point (such as eutectic compounds). This demonstrates that the bonding under transitory liquid phase conditions resulted in the cohesiveness and continuity of the bonding zone. The BNi-2 filler metal melt has been able to wet the adjacent surfaces of the joint well and flow easily on them. The low wetting angle of nickel-base filler metal melts on austenitic stainless steel base metal (10–45°) makes it flow easily on the faying surfaces after melting. In TLP procedure at high-temperatures with long service life, the filler metal must be able to wet the faying surfaces and flow easily to fill the joint. As a result, wetting and spreading the filler metal melt on the components to be jointed is necessary for TLP bonding. However, other factors that affect wetting and spreading include surface conditions (roughness and cleanliness of faying surfaces), TLP conditions (joining atmosphere; bonding temperature, holding time, and joint design), the type of interlayer (amorphous or crystalline filler metal, thickness and chemical composition of interlayer) and physical/chemical reactions between the molten middle layer and base metals [16]. Amorphous filler metals, due to their finer structure and uniform distribution of alloying elements (and even impurities) have been made them widely used in joints with narrow seams

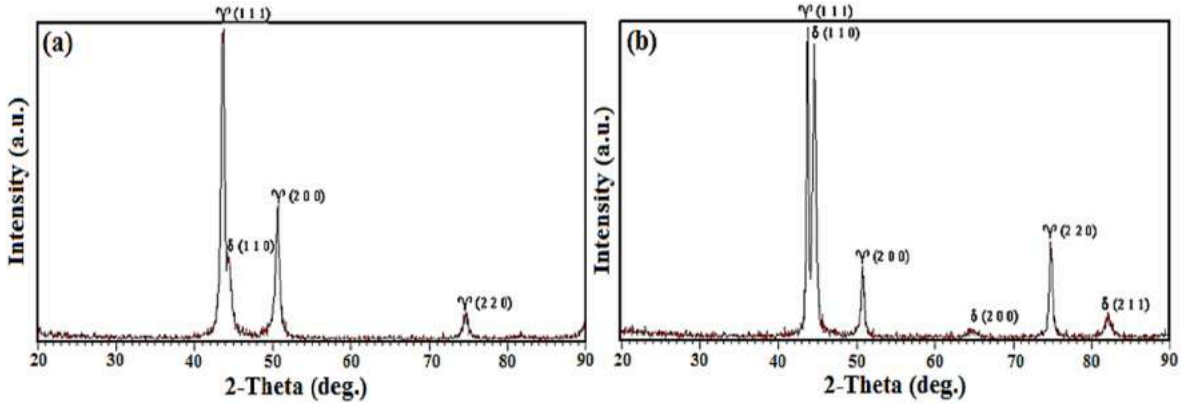

Fig. 5. XRD pattern of austenitic stainless steel 316L at: a) as-received and b) heat-treated at 1080 °C/45 min condition.

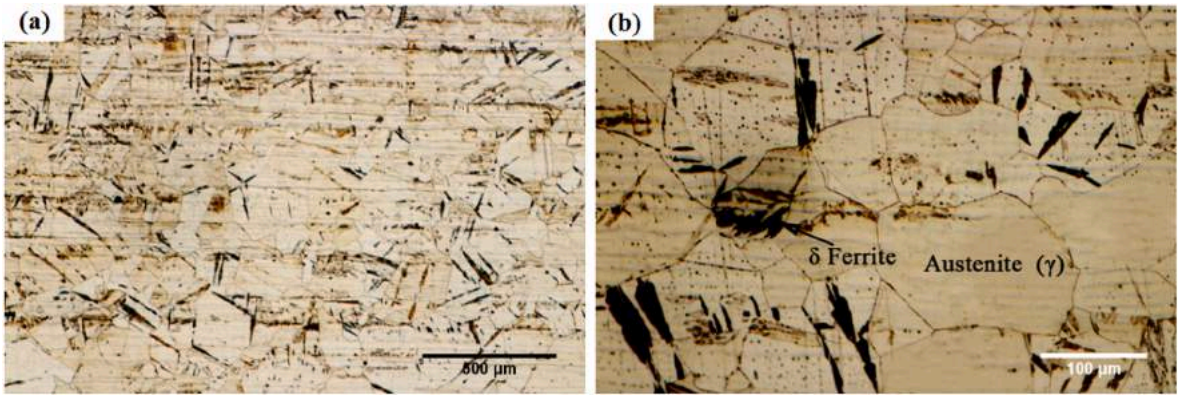

Fig. 6. Optical microscopy of heat-treated austenitic stainless steel 316L at 1080 °C/45 min condition at: a) 50X and b) 200× magnifications.

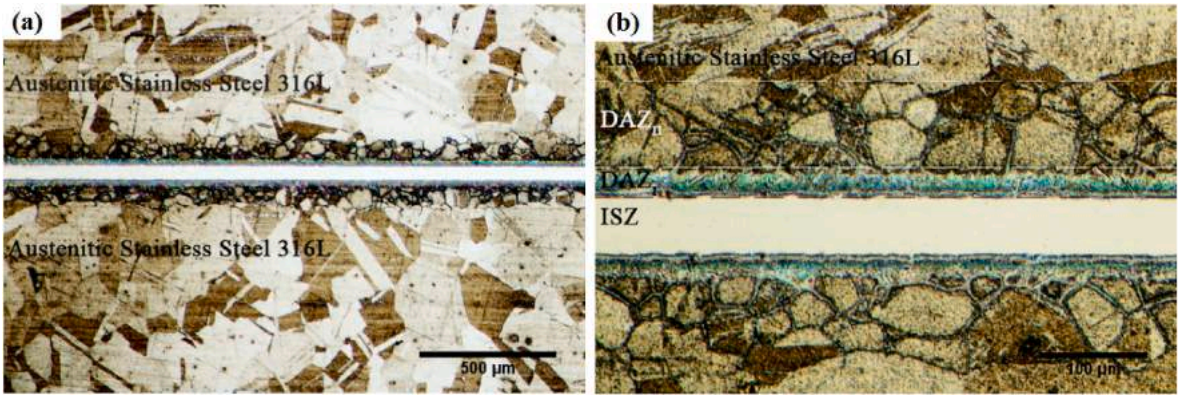

Fig. 7. Optical micrographs of microstructure of TLP bonded stainless steel 316L at 1080 °C/45 min condition at: a) 50X and b) 200X magnifications.

[25]. During heating, they develop a crystalline structure, and when they reach the melting point, they totally melt and flow over the bonding surfaces. According to Cristofaro and Bose [26], nickel-based amorphous brazing alloys have superior properties than crystalline varieties as a result of having better wetting characteristics. Moreover, Zhang et al. [27] examined the wetting characteristics of nickel-based (BNi-2 and BNi-3) and iron-based (Fe78B13Si9) amorphous foils on plain carbon steel. They stated that in the bonding conditions of 1200 °C for 5 s under argon atmosphere, BNi-2 foil showed the best wetting (wetting angle 10°) and spreading compared to amorphous BNi-3 (wetting angle 45°) and Iron base foils. They proved that the superior metallurgical compatibility (high chromium solubility in it and the interaction between chromium and carbon in steel) and the low melting point of 2-BNi are the causes of this wettability.

Fig. 7 also shows that no defects, such as lack of filling of surface imperfections, cracks, holes, or oxide residues have been found in the joining between the base metal and the filler metal, indicating that the joint has been completely filled. Nickel-based filler metals, having anti-oxidant components (such as silicon, phosphorus and boron), break the fine oxide layers of the stainless steel surface and reach the metal surface of the substrate. Finally, increasing the temperature above the liquidus temperature helps helps to reduce the wetting angle and spread easily on the surface of the substrate. The bonding environment has a significant impact on the wetting and spreading of the molten filler metal as well as the bonding quality. In order to improve the joint's quality and lower its contamination, using a vacuum furnace is highly beneficial. At a

bonding temperature of 1135 °C for 300 min, Esmaeili et al. [28] evaluated the impact of the bonding environment (vacuum furnace, argon, and ambient gas) on the bonding quality. According to their claims, some holes emerge during bonding under argon atmosphere and ambient settings, but none were seen while bonding under vacuum. Also, the alloy components diffused between the base metals and the molten interlayer more effectively, which led to higher mechanical characteristics at the vacuum bonding condition. The non-isothermal solidification zone, which is formed due to the lack of enough time for diffusing the melting point depressant elements to base metals and boride and silicate intermetallic compounds in the joint centerline, in addition to reducing the extent of the isothermal solidification zone, they also prevent the precipitation of useful phases (such as $Ni_3(Al, Ti)$ and Ni_3Nb) which will have a destructive effect on mechanical properties. According to Doroudi et al. [29], in their investigation of the fracture sections of the jointed samples of Inconel 625 alloy with BNi-2 interlayer at temperatures of 1025, 1100, and 1175 °C, they stated that the presence of boride compounds in the joint centerline caused a sharp decrease in shear strength properties and brittle fracture mode to predominate. The maximum shear strength (506.15 MPa) was achieved in the bonded sample at a temperature of 1175 °C with a ductile fracture condition by raising the bonding temperature and eliminating boride components. Binesh [30] used a diffusion brazing process to join austenitic stainless steel AISI316L to nickel-based superalloy IN718 with BNi-2 interlayer with thicknesses of 50–150 μm at 1030 °*C* and a holding time of 30 min. Binesh stated that under these joining conditions with a thicker interlayer, pseudo-eutectic intermetallic compounds are continuously formed in the centerline of the joint, which includes the solid solution of γ, Ni_3B, CrB, Cr_2B_3 and Ni_6Si_2B, which leads to a strong reduction in shear strength. The maximum shear strength (440 MPa) was related to the complete isothermal solidification sample, which was broken in a ductile mode.

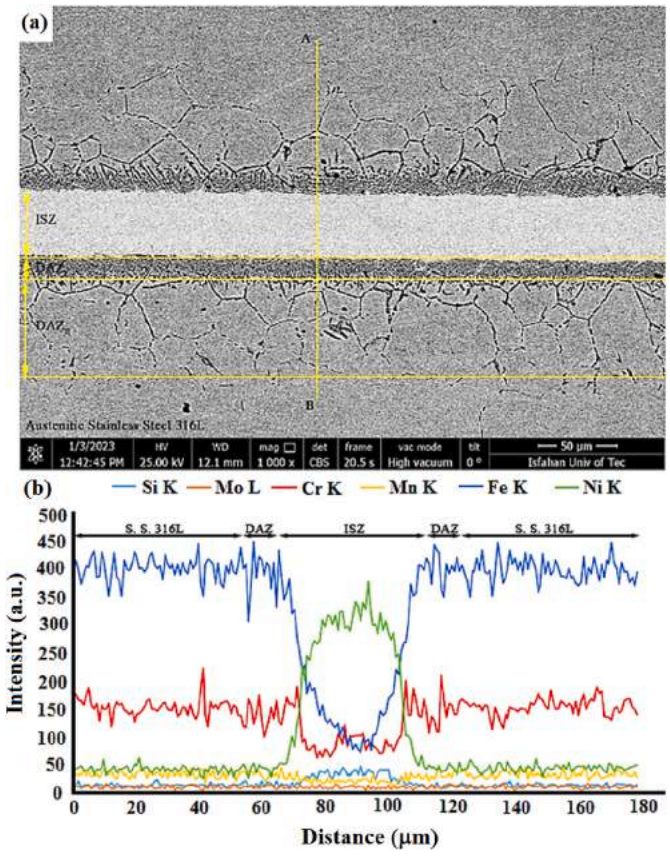

Fig. 8. a) SEM micrograph of TLP bonded stainless steel 316L at 1080 °C/45 min condition and b) Line analysis across the joint gap.

Fig. 8a shows the SEM micrograph along with the linear analysis across the bonding zone. Linear analysis (Fig. 8b) is very useful to investigate the distribution of alloying elements between the base metal (316L) and the solidified interlayer. Since the filler metal is based on nickel, the dispersion of the nickel element is first analyzed. The green lines clearly show where the nickel element is distributed. Nickel is distributed uniformly throughout the base metal of austenitic stainless steel 316L (approximately 10.5 wt%). The nickel content has abruptly risen as one approaches the interlayer/base metal interface. The reason for the lack of increase in nickel concentration in the region adjacent to the joint is due to the accumulation of the nickel element, which is caused by: a) diffusion of the nickel element from the interlayer to the region adjacent to the joint and b) the formation of nickel-rich compounds due to the diffusion of the boron element and the formation of nickel boride intermetallic compounds. Although the holding time was relatively long (45 min), the distribution of the nickel element in the joining area was uneven and accompanied by fluctuations. The distribution of chromium element is uniform before reaching the bonded zone (diffusion-affected zone), but upon reaching the area where the intermetallic compounds are formed continuously and discontinuously, it is strongly associated with fluctuation, so that when the line is crossed scanning the compounds, the concentration of Chromium suddenly increases and then decreases, which indicates the accumulation of chromium element in these compounds. In the area adjacent to the interface, the concentration of chromium increases, and upon reaching the interface, a sudden drop in concentration occurs. Similar to nickel, the distribution of chromium elements in the bonding zone is non-uniform. The base metal is based on the Fe–Ni–Cr alloy system, to which molybdenum, silicon and manganese alloy elements have been added to improve the properties. The peak of the Iron element reveals that it is evenly distributed in the base metal with no change in peak height. Nevertheless, the peak's intensity abruptly rises as it reaches the area near the joint. While the Iron element concentration in the interlayer was relatively low (1.5 wt%), the linear analysis reveals that it is high in the joint region, confirming the diffusion or dissolution of the Iron element from the base metal in the molten layer. The Iron content has reduced as it has gotten closer to the centerline joint, indicating that there hasn't been enough time to achieve homogeneity there. According to the binary phase diagram of iron-nickel [31], these two alloy elements completely dissolve in one another in the molten state and form a uniform molten phase, but during cooling, depending on the chemical composition (the amount of iron in the nickel melt), different phases and occasionally intermetallic compounds are formed. However, the amount of nickel is dominant and no intermetallic compound is formed in the joint. It can be seen that these two elements are completely dissolved through cooling and the formation of the terminal phase (a single-phase solid solution γ(NiFe)) [32,33]. Silicon is another crucial component. The concentration of Silicon element in the base metal is low and has a uniform distribution; when it reaches the joint, its concentration suddenly increases. It is noteworthy that the Silicon element as a melting point depressant element had a uniform distribution in the bonding zone. The interlayer does not contain molybdenum and manganese elements; however, they have a uniform distribution along the seam after joining. It seems that the low concentration of these elements in the base metal has caused that even when they enter the interlayer melt, they can be placed in substantial spaces and distributed uniformly. Based on this, the distribution and accumulation of different alloy elements along the joint seam lead to the creation of microstructural gradients and different regions in the joint, each region having specific characteristics. Therefore, the classification of microstructural areas in the transient liquid phase bonding of austenitic stainless steel L316 with BNi-2 interlayer composed of 1) Isothermal solidification zone, 2) Diffusion-affected zone, and 3) base metal. One of the points that can be seen from Fig. 8a is that the area adjacent to the common phase of the base metal/interlayer interface has two completely different zones in terms of the

distribution of secondary phase compounds: 1) Primary diffusion-affected zone (DAZ_I) and 2) Secondary diffusion-affected zone (DAZ_{II}). In the DAZ_I, the volume fraction of secondary phase compounds is high, and in this region, the compounds are often fine and placed at a very short distance from each other, while in the DAZ_{II}, the secondary phases have a continuous (transgranular) and discontinuous (intergranular) morphology. They are formed at a large distance from each other with a small volume fraction. In the following, each of these microstructural areas is explained in more detail.

3.3.1. Microstructure of isothermal solidification zone

The SEM micrograph of the isothermal solidification zone is shown in Fig. 9a (magnified image of TLP bonded stainless steel 316L in Fig. 8a). The EDS area (A) of the chemical composition of ISZ is presented in Table 3. The research makes it evident that this region is rich in nickel as well as other alloying elements including chromium, iron, manganese, molybdenum, and silicon. Considering that this region is a single phase without the presence of other intermetallic and quasi-eutectic phases, it can be claimed that the isothermal solidification zone consists of a nickel-rich solid solution with a Face Centered Cubic (FCC) structure. When assembly reaches the liquidus temperature of BNi-2 (~1012.3 °C), the interlayer containing melting point depressant (boron and silicon) is completely melted and a region rich in these elements is formed. This melt is placed in contact with the base metal of austenitic stainless steel 316L poor in melting point depressant elements. This difference in concentration causes the slope of the chemical composition. According to the laws governing the process of transient liquid phase bonding, it is necessary to establish thermodynamic equilibrium at the solid/melt interface. Hence, the Iron-rich base metal must be dissolved in the interlayer melt. As a result, the concentration of atoms in the melt that lower the melting point is decreased. This increases the size of the bonding zone [34]. When the width of the bonding zone reaches maximum, equilibrium is established at the solid/melt interface. According to Ghasemi and Pouranvari [35], isothermal solidification will never occur if the interface remains in equilibrium. According to them, the cause for the isothermal solidification of the melt is the departure and rearrangement of thermodynamic equilibrium conditions at the interface. They argued that the chemical composition of the melt remains constant throughout the melt, while the chemical composition of the solid in the interface is not constant and varies with the diffusion of melting point depressant elements, the solid chemical composition in the interface changes. Therefore, in order to create a momentary equilibrium at the interface, it is necessary for the diffusion flow of melting point depressants towards the base metal to occur. With the diffusion of melting point depressant elements from the solid/melt interface, the melt becomes depleted of these elements, and its liquidus temperature rises. As a consequence, the melt temperature is greater than the joining temperature, so isothermal solidification begins, and nickel-rich solid solution dendrites emerge from the solid/melt interface by epitaxial growth towards the centerline joint. Owing to the non-segregation of elements that melting point depressant elements due to their diffusion into the base metal, the formation of destructive intermetallic and quasi-eutectic phases in the joint is prevented [36]. The rate of isothermal solidification is dependent on the diffusion coefficient of the fastest element (boron) from the residual melt in the central joint to the isothermal solidification zone (formed dendrites) and from the isothermal solidification zone to the base metal [37]. The gradient of chemical composition or the gradient of the chemical potential caused by elements which decrease the melting point (especially the element with a higher diffusion coefficient in the base metal, boron) among the base metal and the molten interlayer [38] is the primary driving force in the formation of isothermal solidification zone free of intermetallic compounds. Liu et al. [39] stated in the TLP bonding of austenitic stainless steel 316L with BNi-2 interlayer, considering that the diffusion coefficient of boron element is 4 times higher than the diffusion coefficient of Silicon element. Therefore, they stated that the isothermal solidification of the molten layer depends on the coefficient of boron, and according to the Arrhenius nature of the diffusion coefficient, they proposed the relation for the relationship between the diffusion coefficient and temperature.

Table 3
EDX analysis of various phases indicated in Fig. 9 (wt.%).

Zones	Chemical Composition						Suggested phase
	Ni	Fe	Cr	Mo	Mn	Si	
A	Bal.	15.60	17.42	1.62	0.60	0.46	γ-solid solution
B	Bal.	31	20	1.58	0.86	0.1	Ni-Based Boride
C	6.73	Bal.	19.77	1.44	1.76	0.38	Fe–Cr–Mo Boride
D	5.15	Bal.	26.16	0.59	1.67	0.33	
E	4.86	Bal.	24.14	1.89	1.91	0.58	
F	4.65	Bal.	32.2	2.1	1.56	0.42	

$$D = 1.87 \times 10^{-4} \exp\left\{\frac{-1.34}{RT}\right\} \quad (1)$$

3.3.2. Microstructure of diffusion-affected zone

The most important zone that contains precipitations even with the completion of isothermal solidification is the diffusion-affected zone. Fig. 9b indicates the primary diffusion-affected zone (DAZ_I) and the secondary diffusion-affected zone (DAZ_{II}) along with their extent. In DAZ_I, the fine and irregular bulky precipitations are formed in a compact form with high density. EDS point analysis of various precipitations with different morphologies from the diffusion-affected zone is given in Table 3. The fine one formed right in the DAZ_I/ISZ joint (precipitation B)

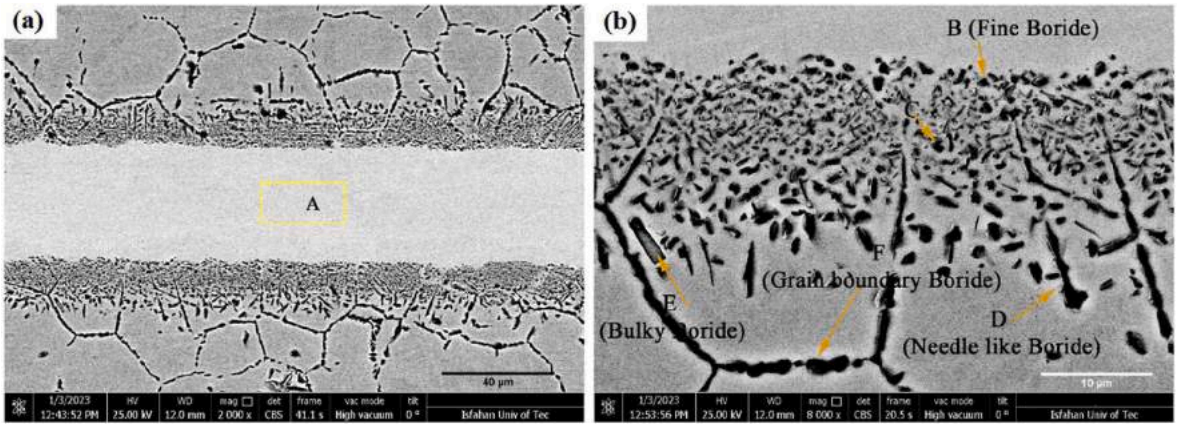

Fig. 9. SEM micrograph of: a) Bonding zone and b) Diffusion-affected zone.

have a dark appearance and blocky morphology, and are rich in nickel, iron, chromium and molybdenum as shown in Fig. 10 (magnified image of the various precipitations in Fig. 9b). Nickel concentration is about 45 wt%, Iron concentration is 31 wt%, chromium concentration is about 20 wt%, and molybdenum is about 2 wt%. These types of precipitations are important because they are formed into fine particles during heating up to the bonding temperature right at the interface and with the passage of time with more absorption of the melting point depressant element with a higher diffusion coefficient (boron element) and reaction with base metal elements (such as iron and molybdenum) become coarse. The high concentration of the nickel element and the presence of these deposits on the side of the interlayer caused these deposits to be formed right where the boron element wanted to enter the base metal, but did not have the necessary energy to diffuse (the heating stage in the solid state). With the complete melting of the interlayer and the dissolution of the substrate, a part of these deposits are dissolved and the rest act as absorption sinks of boron element penetrated during the isothermal solidification stage. At the same time, these deposits interacted with and absorbed components of iron, chromium and molybdenum from the base metal. As a result, the deposit generated is a nickel-iron-chromium-molybdenum boride. Yuan et al. [40] research of microstructural changes and bonding behavior during transient liquid phase bonding of duplex stainless steel with two Ni–B-based interlayers stated that unlike the conventional models in investigating the analytical behavior of the transient liquid phase bonding process, before the dissolution stage of the base metal, a significant diffusion flow of boron from interlayer to the base metal occurs during heating, and this enriches the interface of the interlayer/base metal is made from the boron. Because the activation energy for the boron element to diffuse the base metal is not present at low temperatures, only a small portion of it does so, and the rest of it remains in the interface and is formed as blocky nickel-rich borides as a result of the solid-state reaction. This phenomenon has been observed in the TLP bonding of Cobalt-based superalloy FSX-414 by Bakhtiari et al. [41] and the dissimilar TLP bonding of Cobalt-based superalloys FSX-414 and X-45 by Naalchian et al. [42]. Ruiz et al. [43] stated that these borides are of the first generation that are formed during heating, and most of them are dissolved during the dissolution stage of the base metal, and with the loss of their continuity, the necessary path for boron element diffusion is facilitated to the base metal in the isothermal solidification step. The precipitations in DAZ_I exhibit blocky, fine, and continuous needle morphologies.

As seen in Fig. 9, the precipitations in DAZ_{II} appeared as discontinuous needles and low fine quantities. Mirzaei and Binesh [44] reported that in diffusion brazing stainless steel 304L with a BNi-2 interlayer, the fine blocky particles and continuous and non-continuous needle is created in the diffusion-affected zone, which becomes less dense as they move towards the base metal. According to Khakian et al. [45], Li et al. [46], and Liu et al. [47] stated that the morphology of the precipitations depends on the contraction stresses caused by the solidification of the melt in the interlayer, which decreases with the increase in the distance from the junction and the precipitations become fine and spherical. In addition, it should be noted that the defects of the crystal lattice are also not ineffective in this morphology. For instance, the production of precipitations with fine morphology is influenced by Cottrell's atmosphere, the creation of continuous needle precipitations is influenced by stacking fault defect, and the formation of discontinuous needle precipitations is influenced by grain boundaries [48]. Table 3 provides the results of EDS elemental investigation of precipitations with various morphologies. These deposits, which include the greatest concentrations of iron and chromium, have been shown to have developed in situ from the surrounding material as a result of the boron element's penetration into the base metal from the side of the filler metal. Austenitic stainless steel 316L having strong boride-forming elements such as iron, chromium and molybdenum has the necessary conditions for boride formation. The solubility of boron in the ferrite and austenite structure of iron is about 0.001–0.0025 at. % below 900 °C, and with increasing temperature up to 1072 °C, the solubility of boron in austenite reaches 0.016 at. %, which is very low [49]. Also, there is a significant level of interaction between the atoms of iron, chromium, and molybdenum and the boron elements. According to the iron-boron phase diagram, Fe_2B and FeB phases (with increasing amounts of boron) may develop. In addition, the presence of boron contributes to the stability of the austenite phase in the temperature range of 900–1400 °C and increases the diffusivity of boron [50]. The chromium-boron phase diagram shows the formation of a number of borides, including CrB, $Cr_{15}B_3$, $Cr_{12}B$, $Cr_{14}B_4$ and Cr_4B [51]. According to the iron-chromium-boron phase diagram, CrB and FeB have a high degree of mutual solubility, reaching the chemical composition of $(Cr_{0.6}Fe_{0.4})B$ and $(Cr_{0.8}Fe_{0.2})B$ [52]. Thus, these secondary phase deposits are iron-chromium-molybdenum-rich borides that developed in the diffusion-affected zone of the austenitic stainless steel 316L. The presence of these phases has a significant effect on the chemical composition of the base metal matrix. These particles act like sinks to absorb alloy elements, especially boron. If these deposits are not formed, the area adjacent to the interface will be enriched with boron elements. The boron diffusion capacity from the filler metal to the base metal will decrease and the isothermal solidification time will be longer. The formation of these deposits can reduce the concentration of the boron element in the base metal matrix adjacent to the interface and create suitable paths for the further diffusion of the boron elements to areas far from the base metal. Fig. 11a shows the scanning electron microscope image of grain boundary boride along with the distribution of alloy elements along it. These discontinuous precipitation, which are known as grain boundary borides, are formed as a result of the segregation and absorption of boron element by grain boundaries rich in chromium, iron and molybdenum. According to Fig. 11b, the effect of these precipitations on the amount of absorption of chromium was greater than that of Iron. In such a way that the concentration of chromium increased by approaching the precipitations, which indicates the impoverishment of chromium in the surrounding areas. This decrease in the amount of chromium can have a great effect on strengthening the solid solution of the matrix and corrosion (especially pitting corrosion) [53].

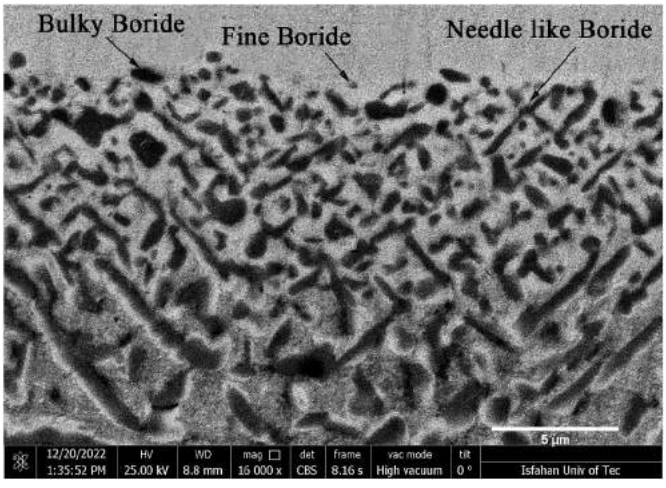

Fig. 10. SEM micrograph of DAZ_I.

3.4. Mechanical properties of joint

3.4.1. Microhardness

Examining the microhardness profile along the joint is one of the crucial factors that sits between the microstructural analysis and the joint's strength characteristics. The distribution of the various phases generated is shown by looking at the microhardness profile, which also validates the microstructural changes that occurred along the jointed

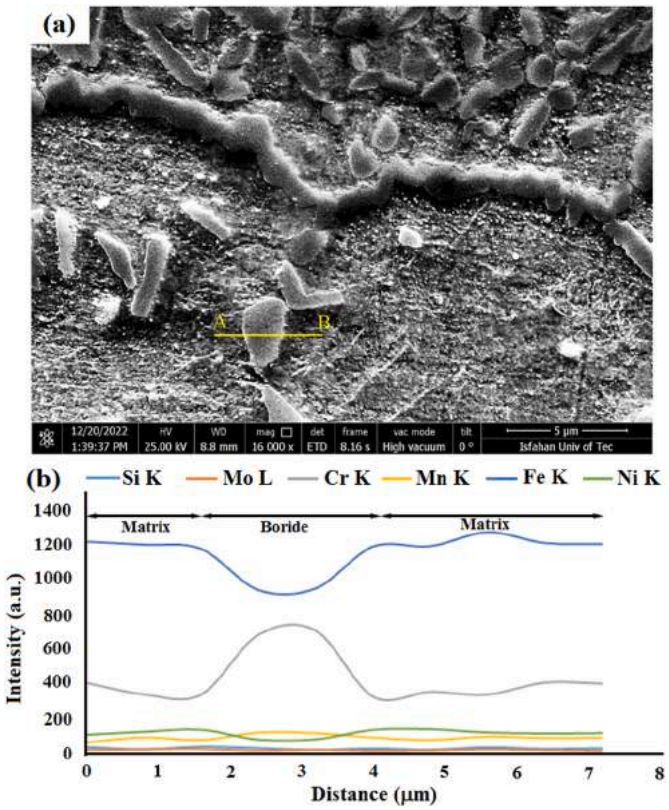

Fig. 11. a) SEM micrograph of grain boundary boride and b) Line scan across the SEM image.

sample. Additionally, it confirms how the alloy components are distributed. Fig. 12 depicts the microhardness profile along the transient liquid phase bonded stainless steel 316L sample. Since the joint is almost symmetrical, just one side of the joint had microhardness measurements done. The austenitic stainless steel 316L with 112 HV_{10} base metal has the lowest amount of hardness. This decrease in hardness is in terms of the softening of the austenitic matrix, and probably the removal of chromium from matrix to form δ ferrite phases. Then, there is an isothermal solidification zone with a hardness of 187 HV_{10} that is comparable to the hardness of the base metal in as-received condition, which could be expected to have a bond strength equivalent to the strength of the base metal. The diffusion-affected zone with iron-chromium base boride secondary phase compounds had the maximum microhardness (302 HV_{10}). Dezfooli et al. [54] when TLP bonding of Inconel 825 to super duplex stainless steel 2750 with BNi-2 interlayer stated that the highest hardness is related to the non-thermal solidification zone (546 HV) after that diffusion-affected zone (super dual phase side 450 HV and Inconel side 302 HV), and the lowest one is due to the isothermal solidification zone (238 HV). They claimed that the formation of eutectic compounds in the centerline joint and boride compounds according to Iron, and nickel in the region close to the joint is the primary cause of this high microhardness. When superalloy Inconel 718 was transient liquid phase bonded to ultrafine-grained austenitic stainless steel 304L with a BNi-2 interlayer, Ghaderi et al. [55] noted that at low temperatures and incomplete isothermal solidification results in microhardness of 425 HV in the joint centerline, even with full isothermal solidification at higher temperatures, the hardness of the isothermal solidification zone (190 HV) compared to the diffusion-affected zone (440 HV) is much less. As a result, the lowest degree of hardness in transient liquid phase bonding is associated with the solidification zone. As previously mentioned, the isothermal solidification zone is a single phase with an austenitic matrix. It is reinforced with a solid solution of iron, chromium, molybdenum, manganese and silicon substantially alloy elements and boron and carbon interstitially. The isothermal solidification zone is similarly strengthened by the grain boundaries; however, it is not as strong as the solid solution. In reality, the isothermal solidification zone is a Ni–Cr–Fe–Mo–Mn–Si alloy, which is made from the initial chemical composition of the filler alloy, the dissolution of the base metal, and the interdiffusion of alloy elements. Iron due to the 3 % difference between the crystal lattice nickel, reduces the stacking fault energy in the nickel base austenitic matrix. Chromium is very effective in resisting corrosion and improving high-temperature strength. In addition, the chromium element is very effective in strengthening the solid solution of the γ matrix, which is due to the difference between its atomic radius with nickel. Chromium causes distortion of the network and production of elastic fields that increase the strength of the solid solution γ, which it does by reducing the stacking fault energy of the nickel matrix. Molybdenum is very effective in solid solution strengthening because it has a much larger atomic radius than nickel. Molybdenum is dissolved in the γ matrix and by increasing its amount, it also increases the high-temperature strength. Finally, manganese is a stabilizer of the austenite phase; although its large amounts reduce the durability of the base alloy, but its presence in small amounts is beneficial [56]. Accordingly, the hardness of the isothermal solidification zone is affected by the presence and amount of alloying elements. Iron is in terms of 3 % difference and this crystal network with nickel decreases the energy of arrangement defects in nickel base austenitic field. Chromium is effective in resisting corrosion and improving high-temperature strength. Besides, the chromium element is effective in strengthening the solid solution of the γ field, which is in terms of the difference between its atomic radius and nickel. Moreover, the hardness of the isothermal freezing zone is affected by the presence and values of alloying elements.

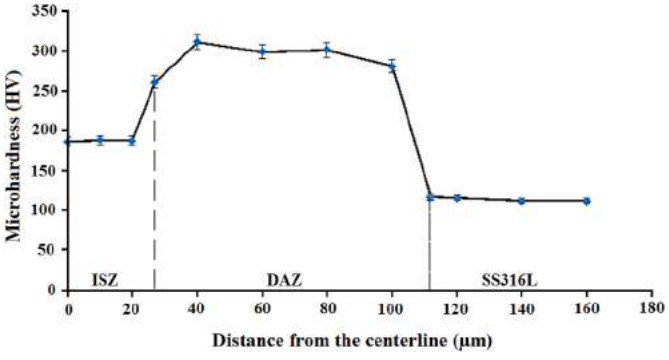

Fig. 12. Microhardness profile across the transient liquid phase bonded stainless steel 316L at 1080 °C/45 min condition.

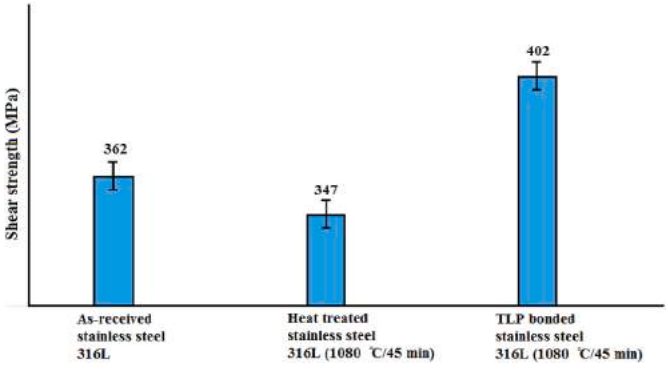

Fig. 13. Comparison of shear strength of base metal (austenitic stainless steel 316L) of as-received, heat-treated and bonding 1080 °C/45 min.

3.4.2. Shear and tensile strength

Fig. 13 compares the shear strength of austenitic stainless steel 316L in its as-received (362 MPa), heat-treated (347 MPa) and bonded (MPa 402) at 1080 °C/45 min conditions. The reduction in shear strength of austenitic stainless steel 316L resulting from exposure to bonding conditions was mostly attributable to grain growth. Nevertheless, the strength of the bonded sample is greater than the strength of the base metal in both the as-received and heat-treated states, and the failure of the sample in the base metal occurred in the diffusion-affected zone. The microstructure of the bonding zone has a substantial influence on the joint samples' strength. The lack of harmful combinations and flaws has a significant effect on achieving maximal shear strength. At the 1080 °C/45 min bonding conditions for achieving full isothermal solidification and interdiffusion of alloy components to obtain the maximum microhardness and, therefore, shear strength in the joint region are met, making failure through the joint area impossible. In the dissimilar joining of austenitic stainless steel 316 to Inconel 718, Salmaliyan and Shamanian [57] reported that when the isothermal solidification is incomplete, the strength of the bonded samples drops sharply due to the presence of brittle compounds and precipitates. Upon the conclusion of isothermal solidification, the shear strength of the joint achieves its maximum (480 MPa), which is 66 % of Inconel 718's shear strength and 29 % higher than stainless steel 316. Owing to the diffusion of boron elements into the regions next to the common phase inside the base metal, boride is generated in the adjacent regions, with a portion of it freely distributed in the grain boundaries and matrix [58]. This element's presence at grain borders inhibits excessive grain development. Therefore, the presence of boron element as a grain boundary strengthening can increase the strength of the base metal adjacent to the diffusion-affected zone, which is the primary reason for the greater strength of the bonded sample relative to the base metal under heat treatment conditions [59]. In the transient liquid phase bonding of nickel-based superalloys Inconel 738 and 718 with BNi-2 interlayer at different temperatures and times, Bakhtiari et al. [60] reported that the effect of the alloying elements of the base metal and the interlayer on solid solution strengthening was dependent on the temperature and bonding time, such that by increasing the time and temperature of the bonding the strengthening components of the solid solution accumulate in the bonding area and contribute to the improvement of the material's strength. As indicated before, the elements molybdenum, chromium, silicon, and iron have a substantial impact on the solid solution strengthening of nickel-based superalloys [61]. As a result, evaluating the microhardness of the isothermal solidification zone is somewhat beneficial for comprehending the causes influencing the variations in shear strength of the joined samples.

Fig. 14a and b shows the SEM micrograph of the fracture surface of the sample bonded at 1080 °C for 45 min. The lack of wide eutectic compounds in the joint centerline, which results in brittle fracture, has led the sample to undergo plastic deformation under shear conditions, and the presence of many fine dimples suggests an entirely ductile fracture. As stated previously, the microhardness of the bonding zone (isothermal solidification) is greater than the microhardness of the base metal [62–67]. Consequently, the shear strength of the joint is greater than that of stainless steel 316L under heat treatment similar to joining conditions. Fig. 14d shows the SEM micrograph of the fracture cross-section of the tensile sample, which reveals the presence and quantity of deep dimples, suggesting an entirely ductile fracture.

The stress-strain curve of the stainless steel 316 sample bonded at 1080 °C for 45 min is shown in Fig. 15. As can be seen, the yield strength and ultimate strength of the joined sample are 260 and 485 MPa, which are roughly similar to 89 % and 82 % of the base metal. Owing to the fact that stainless steel was exposed to temperature and maintenance in the condition of joining, the tensile strength of the jointed sample is similar to the tensile strength of stainless steel in the condition of heat treatment

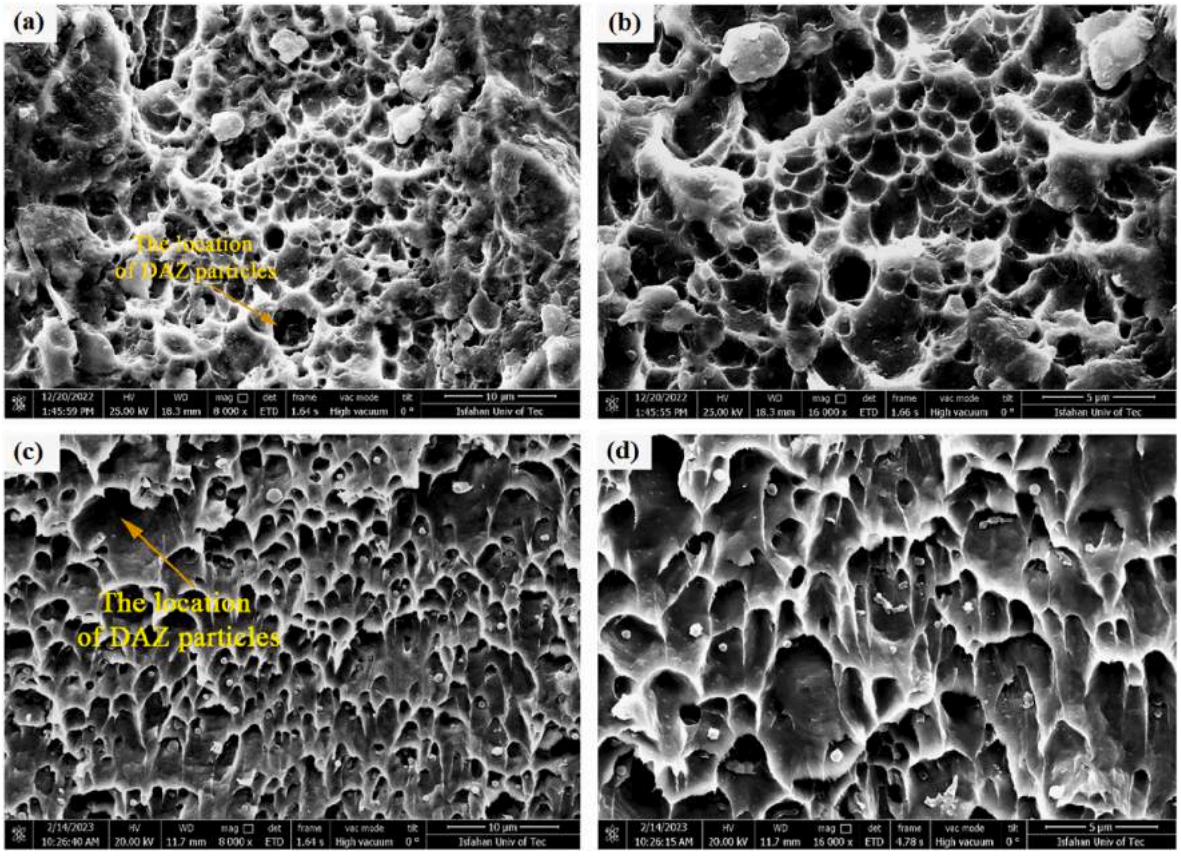

Fig. 14. SEM micrograph of fracture surface of TLP bonded at 1080 °C/45 min condition at: a,b) Shear testing and c,d) Tensile testing.

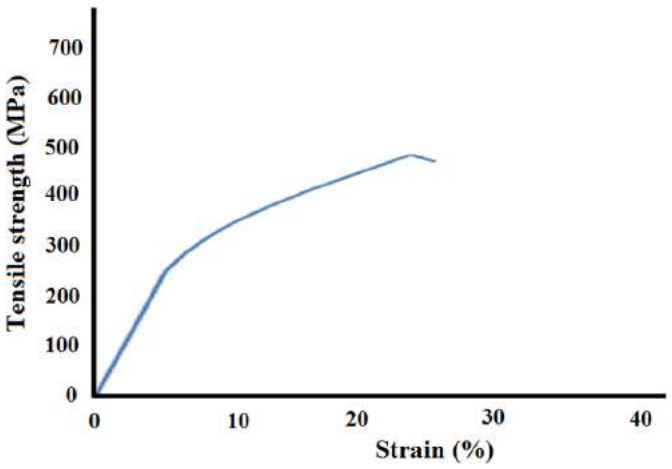

Fig. 15. Tensile-strain curve of TLP bonded austenitic stainless steel 316L by BNi-2 interlayer at 1080 °C/45 min condition.

since the base metal failed [68–74].

4. Conclusions

In this research, along with the joining of the gas turbine fuel nozzle, part from austenitic stainless steel 316L alloy with BNi-2 interlayer by the transient liquid phase bonding process, microstructure test, shear strength, and tensile strength tests have been placed. Microstructural evolution of base metal and bonded samples are investigated by optical and field emission scanning microscopy. The mechanical properties of stainless steel 316L and TLP bonded samples are measured by microhardness, shear and tensile testing. Conclusions drawn from the analysis are as follows:

1- Austenite stainless steel 316L has equiaxed and fine grain with 32 μm grain size. Phase analysis shows that there is very little ferrite phase in its microstructure. Moreover, heat-treated austenite stainless steel 316L at 1080 °C/45 min (bonding condition) resulted in the grain size of the base metal growing (43 μm), which is in terms of recrystallization during heat treatment. The phase analysis of the XRD pattern confirmed the growth of the ferrite structure. The presence of a very small amount of ferrite δ in the context of austenitic stainless steel 316L has acted as a nucleation site for the transformation of the austenite phase to ferrite.

2 The bonding zone is clearly observed as a thin strip with a thickness of 52 μm in the center that shows an increase in the joint width. Also, the observations demonstrate that the bonding zone is devoid of contaminants, holes, cracks, and harmful compounds, such as those with a low melting point. In addition, elemental distribution across the joint shows the classification of microstructural areas in the transient liquid phase bonding of austenitic stainless steel L316 with BNi-2 interlayer is: 1) Isothermal solidification zone, 2) Diffusion-affected zone, and 3) base metal.

3 Owing to the non-segregation of elements that melting point depressant elements due to their diffusion into the base metal, the formation of destructive intermetallic and quasi-eutectic phases in the joint is prevented, and nickel-rich solid solution dendrites (γ) emerge from the solid/melt interface by epitaxial growth towards the centerline joint.

4- The diffusion-affected zone is divided into two areas: DAZ_I and DAZ_{II}. In DAZ_I, the fine and irregular bulky precipitations are formed in a compact form with high density, but the precipitations in DAZ_{II} appear as discontinuous needles and low fine quantities. Also, there are two generations of borides formed in the diffusion-affected zone: the primary generation is nickel-iron-chromium-molybdenum boride. These intermetallic compounds are formed during heating until bonding temperature due to solid state diffusion of boron. And second generation is iron-chromium-molybdenum boride when formed during the isothermal solidification stage.

5 The microhardness profile along the transient liquid phase bonded stainless steel 316L sample has been uniform in each zone. The hardness from the lowest to the highest value is base metal (112 HV_{10}), isothermal solidification zone (187 HV_{10}) and diffusion-affected zone (302 HV_{10}). The increase in hardness is due to the formation of boride deposits. In addition, the shear strength of the bonded sample was 402 MPa, which is approximately 11 % more than the as-received stainless steel 316L. The tensile strength of the bonded sample was 485 MPa, which is approximately 82 % of stainless steel 316L. In both shear and tensile tests, the presence of small dimples indicates the ductile failure of the joint samples in base metal.

Funding

This research received no external funding.

Author contributions

Methodology, formal analysis, writing—original draft preparation, M. Naalchian, J. Manshaee; Conceptualization, supervision, writing—review and editing, M. Kasiri-Asgarani, H. R. Bakhsheshi-Rad. All authors have read and agreed to the published version of the manuscript.

Author statement

All persons who meet authorship criteria are listed as authors, and all authors certify that they have participated sufficiently in the work to take public responsibility for the content, including participation in the concept, design, analysis, writing, or revision of the manuscript. Furthermore, each author certifies that this material or similar material has not been and will not be submitted to or published in any other publication before its appearance in the International journal of pressure vessels and piping.

Declaration of competing interest

The authors declare that they have no known competing financial interests or personal relationships that could have appeared to influence the work reported in this paper.

Data availability

Data will be made available on request.

Acknowledgement

The authors acknowledge the laboratory operators Mrs. Fooladgar and Mr. Parastegari and Iran Brazing Group for their assistance in using laboratory equipment.

References

[1] A. Backhouse, N. Baddoo, Recent developments of stainless steels in structural applications, CE/Papers 4 (2–4) (2021) 2349–2355.
[2] N.R. Baddoo, Stainless steel in construction: a review of research, applications, challenges and opportunities, J. Constr. Steel Res. 64 (2008) 1199–1206.
[3] M. Durand-Charre, Microstructure of Steels and Cast Irons, Springer Science & Business Media, 2004.
[4] T. Voisin, R. Shi, Y. Zhu, Z. Qi, M. Wu, S. Sen-Britain, Y. Zhang, S.R. Qiu, Y. M. Wang, S. Thomas, Pitting corrosion in 316L stainless steel fabricated by laser

powder bed fusion additive manufacturing: a review and perspective, JOM 74 (2022) 1668–1689.
[5] M. Aghakhani, E. Mehrdad, E. Hayati, Parametric optimization of gas metal arc welding process by Taguchi method on weld dilution, Int. J. Model. Optim. 1 (2011) 216.
[6] R. Martins, C. Branco, A. Gonçalves-Coelho, E. Gomes, Metallurgical study of a AISI 316L stainless steel used in a gas turbine exhaust system, Mater. Sci. Forum 514–516 (2006) 1521–1525.
[7] P.J. Maziasz, R.W. Swindeman, J.P. Montague, M. Fitzpatrick, P.F. Browning, J. F. Grubb, R.C. Klug, R. Painter, Stainless steel foil with improved creep-resistance for use in primary surface recuperators for gas turbine engines, Materials Solutions 98 (1998) 70–78.
[8] T. Ginter, T. Bouvay, Uprate options for the MS7001 heavy duty gas turbine, GE paper GER-3808C, GE Energy 12 (2006).
[9] M.B. Henderson, D. Arrell, R. Larsson, M. Heobel, G. Marchant, Nickel based superalloy welding practices for industrial gas turbine applications, Sci. Technol. Weld. Join. 9 (2004) 13–21.
[10] S. Sravan Sashank, S. Rajakumar, R. Karthikeyan, Dissimilar welding of austenitic and martensitic stainless steel joints for nuclear applications: a review, E3S Web Conf. 309 (2021).
[11] F. Dokme, M.K. Kulekci, U. Esme, Microstructural and Mechanical Characterization of Dissimilar Metal Welding of Inconel 625 and AISI 316L, Metals, 2018.
[12] M. Hathesh, A review on welding related problems and remedy of austenitic stainless steels, IRJET, Int. Res. J. Eng. Technol. (2020).
[13] V.P. Kujanpää, S.A. David, C.L. White, Formation of hot cracks in austenitic stainless steel welds–solidification cracking, Weld. J. 65 (1986) 203s–212s.
[14] D.J. Kemmenoe, E.A. Theisen, S.P. Baker, Strength of 444 stainless steel single-lap joints brazed with Ni-based metallic glass foils for corrosive environments, Metall. Mater. Trans. 53 (2022) 1407–1418.
[15] H. Zhang, W. Zhu, T. Zhang, C. Guo, X. Ran, Effect of brazing temperature on microstructure and mechanical property of high nitrogen austenitic stainless steel joints brazed with Ni–Cr–P filler, ISIJ Int. 59 (2019) 300–304.
[16] G.O. Cook Iii, C.D. Sorensen, Overview of transient liquid phase and partial transient liquid phase bonding, J. Mater. Sci. 46 (2011) 5305–5323.
[17] M. Emami, B. Binesh, J.M. Heydarzadeh, Analysis of microstructure, kinetics of isothermal solidification and mechanical properties of IN718/MBF-20/SS316L TLP joints, Phil. Mag. 101 (2021) 1726–1749.
[18] A.Y. Shamsabadi, R. Bakhtiari, G. Eisaabadi B, TLP bonding of IN738/MBF20/IN718 system, J. Alloys Compd. 685 (2016) 896–904.
[19] H. Tazikeh, S.E. Mirsalehi, A. Shamsipur, Relationship of isothermal solidification completion and precipitate formation with mechanical properties of Inconel 939 joints vacuum TLP bonded by an amorphous Ni–Cr–Fe–Si–B filler alloy, J. Mater. Res. Technol. 18 (2022) 4762–4774.
[20] M. Naalchian, M. Kasiri, M. Shamanian, R. Bakhtiari, H. Bakhsheshi-Rad, Effect of substrate's heat treatment on microstructure and mechanical properties TLP bonding of dissimilar X-45/FSX-414 cobalt based superalloys, Met. Mater. Int. 27 (2021) 4657–4668.
[21] M. Landowski, A. Świerczyńska, G. Rogalski, D. Fydrych, Autogenous fiber laser welding of 316L austenitic and 2304 lean duplex stainless steels, Materials 13 (2020) 2930.
[22] M.K. Herliansyah, P. Dewo, M.H.N.E. Soesatyo, W. Siswomihardjo, The Effect of Annealing Temperature on the Physical and Mechanical Properties of Stainless Steel 316L for Stent Application, IEEE, 2015, pp. 22–26.
[23] K. Saeidi, X. Gao, F. Lofaj, L. Kvetková, Z.J. Shen, Transformation of austenite to duplex austenite-ferrite assembly in annealed stainless steel 316L consolidated by laser melting, J. Alloys Compd. 633 (2015) 463–469.
[24] A. Bakhtiari, I. Berenjani, Influence of annealing heat treatment on pitting corrosion resistance of stainless steel type 316, J. Inst. Eng. 20 (2) (2014) 97–106.
[25] W. Yu, W. Lu, T. Xia, Formation process of joints brazing with amorphous filler metal, Rare Met. Mater. Eng. 42 (2013) 688–691.
[26] N.J. De Cristofaro, A. Datta, Rapidly Solidified Filler Metals in Brazing and Soldering Applications, 1985, pp. 1715–1722.
[27] G.F. Zhang, J.X. Zhang, Y. Pei, J. Xu, Wetting behavior of nickel based and iron based amorphous filler metal foil on plain carbon steel pipe, in: Hanjie Xuebao/Transactions of the China Welding Institution, 27, 2006, pp. 61–64.
[28] H. Esmaeili, S.E. Mirsalehi, A. Farzadi, Effect of joining atmosphere in transient liquid phase bonding of inconel 617 superalloy, Metall. Mater. Trans. B 48 (2017) 3259–3269.
[29] A. Doroudi, A. Ebrahimzadeh Pilehrood, M. Mohebinia, A. Dastgheib, A. Rajabi, H. Omidvar, Effect of the isothermal solidification completion on the mechanical properties of Inconel 625 transient liquid phase bond by changing bonding temperature, J. Mater. Res. Technol. 9 (2020) 10355–10365.
[30] B. Binesh, Diffusion brazing of IN718/AISI 316L dissimilar joint: microstructure evolution and mechanical properties, J. Manuf. Process. 57 (2020) 196–208.
[31] T.B. Massalski, Binary Alloy Phase Diagrams, 1990.
[32] G. Cacciamani, A. Dinsdale, M. Palumbo, A. Pasturel, The Fe–Ni system: thermodynamic modelling assisted by atomistic calculations, Intermetallics 18 (2010) 1148–1162.
[33] G.I. Silman, Compilative Fe – Ni phase diagram with author's correction, Met. Sci. Heat Treat. 54 (2012) 105–112.
[34] W.D. MacDonald, T.W. Eagar, Transient liquid phase bonding, Annu. Rev. Mater. Sci. 22 (1992) 23–46.
[35] A. Ghasemi, M. Pouranvari, Thermal processing strategies enabling boride dissolution and gamma prime precipitation in dissimilar nickel-based superalloys transient liquid phase bond, Mater. Des. 182 (2019), 108008.
[36] M. Ajabshiri, M. Shamanian, A. Ashrafi, M.A. Karimi, The effect of bonding time on dissimilar joint properties between inconel 625 and AISI 316L using transient liquid phase bonding method with Cu interlayer, J. Mater. Eng. Perform. 31 (2022) 3311–3325.
[37] V. Jalilvand, H. Omidvar, H.R. Shakeri, M.R. Rahimipour, A study on the effect of process parameters on the properties of joint in TLP-bonded inconel 738LC superalloy, Metall. Mater. Trans. B 44 (2013) 1222–1231.
[38] O.A. Idowu, N.L. Richards, M.C. Chaturvedi, Effect of bonding temperature on isothermal solidification rate during transient liquid phase bonding of Inconel 738LC superalloy, Mater. Sci. Eng. 397 (2005) 98–112.
[39] Z.P. Liu, G.Y. Zhou, F.Q. Tian, D.Q. Chen, S.T. Tu, Experimental investigation on the kinetic parameters of diffusion component for vacuum brazing SS316L/BNi-2/SS316L joint, Proc. Eng. 130 (2015) 497–508.
[40] X. Yuan, M.B. Kim, C.Y. Kang, Microstructural evolution and bonding behavior during transient liquid-phase bonding of a duplex stainless steel using two different Ni-B-based filler materials, Metall. Mater. Trans. A 42 (2011) 1310–1324.
[41] R. Bakhtiari, A. Ekrami, T.I. Khan, The effect of TLP bonding temperature on microstructural and mechanical property of joints made using FSX-414 superalloy, Mater. Sci. Eng. 546 (2012) 291–300.
[42] M. Naalchian, M. Kasiri-Asgarani, M. Shamanian, R. Bakhtiari, H.R. Bakhsheshi-Rad, Comprehensive microstructural investigation during dissimilar transient liquid phase bonding cobalt-based superalloys by BNi-9 amorphous interlayer foil, J. Mater. Res. Technol. 13 (2021) 2144–2160.
[43] J. Ruiz-Vargas, N. Siredey-Schwaller, N. Gey, P. Bocher, A. Hazotte, Microstructure development during isothermal brazing of Ni/BNi-2 couples, J. Mater. Process. Technol. 213 (2013) 20–29.
[44] S. Mirzaei, B. Binesh, Microstructure evolution mechanism and corrosion behavior of transient liquid phase bonded 304L stainless steel, Met. Mater. Int. 27 (2020).
[45] M. Khakian, S. Nategh, S. Mirdamadi, Effect of bonding time on the microstructure and isothermal solidification completion during transient liquid phase bonding of dissimilar nickel-based superalloys IN738LC and Nimonic 75, J. Alloys Compd. 653 (2015) 386–394.
[46] W. Li, T. Jin, X.F. Sun, Y. Guo, H.R. Guan, Z.Q. Hu, Study of Ni-Cr-Co-W-Mo-B interlayer alloy and its bonding behaviour for a Ni-base single crystal superalloy, Scripta Mater. 48 (2003) 1283–1288.
[47] J.D. Liu, T. Jin, N.R. Zhao, Z.H. Wang, X.F. Sun, H.R. Guan, Z.Q. Hu, Effect of Temperature on Formation of Borides in TLP Joint of a Kind of Nickel-Base Single Crystal Superalloy, Materials Science Forum, 2007, pp. 1245–1248.
[48] S.Y. Wang, Y. Sun, X.Y. Hou, C.Y. Cui, X.F. Sun, Y.Z. Zhou, Borides of preferred orientation formed in the transient liquid phase joint of γ′-strengthened Co-base single crystal superalloy, Mater. Lett. 246 (2019) 190–194.
[49] P.E. Busby, M.E. Warga, C. Wells, Diffusion and solubility of boron in iron and steel, JOM 5 (1953) 1463–1468.
[50] J. Miettinen, G. Vassilev, Thermodynamic Description of Ternary Fe-B-X Systems. Part 1: Fe-B-Cr, Archives of Metallurgy and Materials (No 2 June), 2014.
[51] Q. Zhai, J. Xu, T. Lu, Y. Xu, Research on interlayer alloys for transient liquid phase diffusion bonding of single crystal nickel base superalloy DD6, J. Mater. Sci. Chem. Eng. (2014) 12–19, 02.
[52] A. Bondar, Boron-Chromium-Iron: Datasheet from Landolt-Börnstein - Group IV Physical Chemistry · Volume 11D1: "Iron Systems, Part 1" in SpringerMaterials (https://doi.org/10.1007/978-3-540-69761-9-17), Springer-Verlag Berlin Heidelberg..
[53] X. Yuan, M.B. Kim, Y.H. Cho, C.Y. Kang, Microstructures, mechanical and chemical properties of TLP-bonded joints in a duplex stainless steel with amorphous Ni-based insert alloys, Metall. Mater. Trans. 43 (2012) 1989–2001.
[54] M.S. Dezfooli, M. Shamanian, M.A. Golozar, The effect of bonding time on the microstructure and mechanical properties of dissimilar transient liquid phase bonding between UNS N08825 alloy and UNS S32750 super duplex stainless steel using the BNi-2 interlayer, J. Manuf. Process. 64 (2021) 464–472.
[55] S. Ghaderi, F. Karimzadeh, A. Ashrafi, Evaluation of microstructure and mechanical properties of transient liquid phase bonding of Inconel 718 and nano/ultrafine-grained 304L stainless steel, J. Manuf. Process. 49 (2020) 162–174.
[56] D.K. Ganji, G. Rajyalakshmi, Influence of alloying compositions on the properties of nickel-based superalloys: a review, in: H. Kumar, P.K. Jain (Eds.), Recent Advances in Mechanical Engineering, Springer Singapore, Singapore, 2020, pp. 537–555.
[57] M. Salmaliyan, M. Shamanian, Microstructure and mechanical characterization study in the IN718/BNi-2/316L joint by transient liquid phase bonding process, Adv. Mater. Lett. 10 (2019) 663–670.
[58] E. El-Kashif, K. Asakura, T. Koseki, K. Shibata, Effects of boron, niobium and titanium on grain growth in ultra high purity 18% Cr ferritic stainless steel, ISIJ Int. 44 (2004) 1568–1575.
[59] M. ÇetİN, E. Ölmez, Effect of Boron Addition on Mechanical Properties of Cast AISI 304 Stainless Steel, 2018.
[60] R. Bakhtiari, A. Yarmou Shamsabadi, K. Alipour Moradi, Shear strength/microstructure relationship for dissimilar IN738/IN718 TLP joints, Weld. World 64 (2020) 219–231.
[61] H.A. Roth, C.L. Davis, R.C. Thomson, Modeling solid solution strengthening in nickel alloys, Metall. Mater. Trans. A 28 (1997) 1329–1335.
[62] M. Handbook, John lelandand the'Briton brykes, antiquaries journal (1990) Harris, Oliver, in: ASM InternationalHandbook Committee, ASM International, vol. 1MaterialsPark, OH, 2007, pp. 346–356, 87.
[63] K. Esmaeili, L. Wang, T.J. Harvey, N.M. White, W. Holweger, Electrical discharges in oil-lubricated rolling contacts and their detection using electrostatic sensing technique, Sensors 22 (2022) 392.

[64] B. Zhang, W. Wan, A transient-features-based diagnostic method of multi incipient cracks in pipeline systems, Int. J. Pres. Ves. Pip. 199 (2022), 104701.
[65] C. Köse, Effect of heat input and post weld heat treatment on the texture, microstructure and mechanical properties of laser beam welded AISI 317L austenitic stainless steel, Mater. Sci. Eng. 855 (2022), 143966.
[66] C. Köse, Heat treatment and heat input effects on the dissimilar laser beam welded AISI 904L super austenitic stainless steel to AISI 317L austenitic stainless steel: surface, texture, microstructure and mechanical properties, Vacuum 205 (2022), 111440.
[67] V. Garcia-Garcia, Microstructural and mechanical analysis of double pass dissimilar welds of twinning induced plasticity steel to austenitic/duplex stainless steels, Int. J. Pres. Ves. Pip. 198 (2022), 104665.
[68] O. Obeid, A.J. Leslie, A.G. Olabi, Influence of girth welding material on thermal and residual stress fields in welded lined pipes, Int. J. Pres. Ves. Pip. 200 (2022), 104777.
[69] V. Bhanu, A. Malakar, A. Gupta, C. Pandey, Electron beam welding of P91 steel and incoloy 800HT and their microstructural studies for advanced ultra super critical (AUSC) power plants, Int. J. Pres. Ves. Pip. 205 (2023), 105010.
[70] F. Hosseinzadeh, B. Tafazzoli-Moghaddam, H.K. Kim, et al., Residual stresses in austenitic thin-walled pipe girth welds: manufacture and measurements, Int. J. Pres. Ves. Pip. 206 (2023), 105016.
[71] J. Shingledecker, J.J. deBarbadillo, R. Gollihue, E. Griscom, D. Purdy, A. Bridges, Development and performance of INCONEL® alloy 740H® seam-welded piping, Int. J. Pres. Ves. Pip. 202 (2023), 104875.
[72] H. Fan, P. Liu, X. Guo, X. Wang, Y. Wang, Microstructures and properties of a novel 115 mm thick 08Cr9W3Co3VNbCuBN heat-resistant steel tube joints welded by shielded metal arc welding, Int. J. Pres. Ves. Pip. 202 (2023), 104918.
[73] M. Naalchian, M. Kasiri-Asgarani, M. Shamanian, R. Bakhtiari, et al., Phase Formation during heating of amorphous nickel-based BNi-3 for joining of dissimilar cobalt-based superalloys, Materials 14 (2021) 4600.
[74] M. Hafizi, M. Kasiri-Asgarani, M. Naalchian, H.R. Bakhsheshi-Rad, F. Berto, The effect of holding time on dissimilar transient liquid-phase-bonded properties of super-ferritic stainless steel 446 to martensitic stainless steel 410 using a nickel-based interlayer, Micromachines 13 (2022) 1801.